Journal of Engineering and Technology for Industrial Applications

ITEGAM-JETIA

Manaus, v10. n.50, p. 128-137. November/ December., 2024.

DOI: https://doi.org/10.5935/jetia.v10i50.947

ISSN ONLINE: 2447-0228

RESEARCH ARTICLE ACCESS

OPEN

EFR-NET: ENHANCED FRACTURE PREDICTION IN OSTEOPOROSIS WITH U-NET-BASED ANALYSIS

Vidhya K[1], T.M. Thiyagu[2], Edward Naveen V[3], Jenefa A[*4]

[1] Karunya Institute of Technology and Sciences, Coimbatore.
[2] Vel Tech Rangarajan Dr. Sagunthala R&D Institute of Science and Technology, Avadi, Chennai.
[3] Sri Shakthi Institute of Engineering and Technology, Coimbatore.
[4] Karunya Institute of Technology and Sciences, Coimbatore.

[1] http://orcid.org/0000-0002-5439-6202, [2] http://orcid.org/0000-0002-4902-3153, [3]http://orcid.org/0000-0003-5845-2173, [4] http://orcid.org/0000-0002-6697-1788

Email: vidhyak@karunya.edu, t.m.thiyagu@gmail.com, edwanx@gmail.com, jenefaa@karunya.edu

ARTICLE INFO

Article History
Received: November 11, 2023
Revised: December 1, 2023
Accepted: December 10, 2024
Published: December 31, 2024

Keywords:
Deep Learning,
Fracture Prediction,
Osteoporosis,
Medical Imaging,
Image Analysis.

ABSTRACT

Osteoporosis, a prevalent bone disease, is characterized by the equation $B_d = B_m - O_r$, where B_d is bone density, B_m is maximum bone density, and O_r is osteoporosis rate. Conventional imaging techniques, governed by the formula $A_c = I_t\, X\, S_r$ where $A_c$accuracy is, I_t is image thresholding, and S_r is scan resolution), often yield a detection accuracy of merely 75%. In this work, we introduce the EFR-Net: a U-Net-based deep learning model. Its efficacy is represented by the equation $A_n = F_p\, X\, D_c + N_r$, where A_n is the new accuracy, F_p is the fraction of fracture-prone regions detected, D_c is the Dice coefficient, and N_r is the noise reduction factor. Leveraging a comprehensive dataset of 10,000 bone scans, our model, adhering to the above equation, achieved a commendable accuracy rate of 89%. This translates to a mathematical improvement represented by $\Delta A = A_n - A_c$, yielding a 14% enhancement over traditional methods. Moreover, the reduction in false negatives, a critical metric in medical diagnoses, can be quantified by $R_f = \frac{F_{old} - F_{new}}{F_{old}}$, where F_{old} and F_{new} are the old and new false negatives respectively. EFR-Net's innovative approach and promising results underline its potential in revolutionizing osteoporosis-related fracture prediction, offering a robust bridge between computational advancements and clinical necessities.

I. INTRODUCTION

Osteoporosis is a degenerative bone disease that represents a major public health concern, affecting millions worldwide. This ailment weakens bones over time, resulting in them becoming fragile and consequently more susceptible to fractures. The dire repercussions of osteoporosis, ranging from decreased mobility to increased mortality, make early and accurate detection not just a clinical necessity, but also a societal imperative.

Traditional diagnostic techniques for osteoporosis predominantly rely on measuring bone mineral density (BMD). However, BMD measurements, while indicative, are not definitive predictors of fracture risks. Many individuals with osteoporosis remain undiagnosed due to the limitations of current methods. These methods' inability to capture intricate bone patterns, micro-architectural deterioration, and other subtle cues indicative of fracture risks has left a significant diagnostic gap in osteoporosis care.

Conventional osteoporosis detection primarily utilizes dual-energy x-ray absorptiometry (DEXA) scans to measure BMD. Governed by the equation $A_c = I_t\, X\, S_r$, where A_c represents the diagnostic accuracy, I_t the image thresholding, and S_r the scan resolution, DEXA results serve as the gold standard for osteoporosis diagnosis. However, while DEXA scans offer quantitative insights into bone density, they often fall short in providing a holistic understanding of bone quality, which is equally crucial.

In response to the limitations of conventional methods, we introduce EFR-Net, a state-of-the-art U-Net-based deep learning model, tailored specifically for enhanced osteoporosis detection. EFR-Net, by emphasizing fracture-prone regions and capturing micro-architectural nuances in bone scans, aims to revolutionize osteoporosis diagnosis. Its underlying principle can be articulated by $A_n = F_p\ X\ D_c + N_r$, wherein it's designed to amalgamate both quantitative and qualitative aspects of bone health, promising a significant leap over traditional diagnostic paradigms.

Our work in this paper stands out due to several pivotal contributions:

- The inception of EFR-Net, a pioneering deep learning approach, crafted with the nuances of osteoporosis detection in mind.
- A rigorous and comprehensive comparative evaluation against conventional methods, establishing the clear superiority of EFR-Net in terms of diagnostic precision.
- An exhaustive exploration of our dataset, underlining its diverse, representative, and clinically-relevant nature.
- Probing insights into the broader real-world applications, scalability, and clinical implications of deploying EFR-Net in mainstream healthcare systems.

The subsequent sections of this paper have been meticulously organized for clarity and coherence. Section 2 furnishes a thorough review of extant literature and related works. Section 3 delves deep into our proposed methodology, elucidating both the dataset intricacies and the architectural nuances of EFR-Net. Section 4 is dedicated to our experimental results, discussions, and the insights derived therefrom. We finally wrap up with Section 5, where we conclude our findings and shed light on prospective research directions and broader implications.

II. RELATED WORK

Osteoporosis detection and related bone health diagnostics have witnessed a surge in advancements with the integration of deep learning techniques. Pioneered a diagnostic model grounded on an improved deep U-Net network, showcasing the adaptability of U-Net architectures for intricate tasks like osteoporosis gradation. In a similar vein [1], integrated attention units within a modified U-Net architecture, highlighting its efficacy in DEXA and X-ray image diagnostics. The versatility of the U-Net model was further underlined by [2], who adopted multitask learning for the detection of osteoporotic vertebral compression fractures in lumbar spine lateral radiographs. The importance of segmentation in osteoporosis detection was emphasized by [3], who automated the segmentation of vertebral cortex utilizing a 3D U-Net-based deep convolutional neural network [4].

Provided an extensive survey on computer-aided diagnosis systems, offering a panoramic view of the advancements and challenges in osteoporosis detection [5]. As segmentation continues to play a pivotal role [6] showcased an innovative method for the automatic segmentation of the femur and tibia bones from X-ray images, leveraging a pure dilated residual U-Net. The broader implications of deep learning in orthopedic disease diagnostics were elaborated upon by [7], who presented both the current applications and future potential of the technology.

The significance of segmentation in bone health diagnostics was further cemented by [8] through their deep learning method for the automatic segmentation of the proximal femur from quantitative computed tomography images. Proposed a multi-objective segmentation method for bone age assessment using a parameter-tuned U-net architecture [9]. Presented a fusion of machine learning for femur segmentation from CT scans with autonomous finite elements for orthopedic and endocrinology applications [10]. Introduced a Merged U-Net approach for the segmentation of bone tumors in X-ray images [11]. Developed QCBCT-NET for direct measurement of bone mineral density from quantitative cone-beam CT using a human skull phantom study [12]. Highlighted an approach for intervertebral disc labeling incorporating learning shape information for improved accuracy [13]. Introduced an artificial intelligence-based system (AIBMS) for the detection of sarcopenia using deep learning techniques [14].

Reviewed deep convolutional neural network architectures tailored for medical image segmentation tasks [15]. Explored spine MRI segmentation using advanced deep learning techniques [16]. Investigated the predictive value of vertebral body cortical thickness for osteoporosis using opportunistic CT imaging [17]. offered a literature review on osteolysis, covering its basic science and potential computer-based image processing detection methods [18]. Proposed an edge-enhanced instance segmentation approach for wrist CT images leveraging a semi-automatic annotation database [19]. Conducted a systematic review on deep learning applications in dental and maxillofacial image analysis [19]. Predicted bone healing around dental implants under varying conditions using a deep learning network [19]. Introduced ST-V-Net, a method to incorporate shape priors into CNNs for enhanced proximal femur segmentation [22].

Focused on diagnosing osteoporosis using transfer learning techniques within the same domain [22]. Automated the measurement of cortical thickness in the mandibular condyle head using CBCT images via deep learning [24], evaluated deep learning-based quantitative CT for opportunistic osteoporosis screening [25].

However, despite these monumental advancements, traditional methods and several deep learning models have been observed to exhibit certain limitations, especially when it comes to capturing intricate bone patterns, micro-architectural deteriorations, and nuanced indicators of fracture risks. These challenges have culminated in a diagnostic gap in osteoporosis care. In our proposed work, we seek to address and overcome these limitations. By amalgamating both quantitative and qualitative aspects of bone health diagnostics, our solution aims to bridge the existing gaps and present a more comprehensive and robust solution, marking a significant departure from conventional paradigms.

II.1 PROBLEM FORMULATION

The formulation of the osteoporosis detection problem is rooted in a blend of mathematical and statistical methodologies. By grounding our research in these foundational principles, we seek to achieve both clarity in representation and rigor in analysis.
Key Notations
We begin by outlining the primary notations that will be recurrently used:

- B - Bone scan image.
- O- Osteoporosis severity score.
- F - Fracture-prone region in bone scan.
- D_c - Dice coefficient for model accuracy.
- N_r - Noise reduction factor in image.

Problem Definition

Given a bone scan image B, the objective is to predict the osteoporosis severity score O and identify the fracture-prone regions F. Formally, the problem can be defined as:

Predict: $O = f(B)$

Identify: $F = g(B)$

Where f and g are mapping functions that the EFR-Net model learns.

Optimization Objective

The primary optimization goal is to maximize the Dice coefficient D_c while simultaneously minimizing the noise N_r in the predicted fracture-prone regions. This can be mathematically represented as:

$$\max_{f,g} D_c \; subject\ to\ N_r \leq \varepsilon$$

where ε is a predefined threshold for acceptable noise. In the subsequent sections, we will delve deeper into the mechanisms by which we achieve this optimization objective and the empirical results substantiating our methodology.

Table 1: Algorithm: EFR-Net for Osteoporosis Fracture Prediction

FUNCTION $EFR-Net(I)$:
- Initialize U-Net architecture with depth d
- $C_{encoder} \leftarrow Encoder(I)$
- $S \leftarrow Decoder(C_{encoder})$
- **RETURN** S
FUNCTION $Encoder(I)$:
- $E(I) \leftarrow C_{encoder}$ (Encode image I to feature map $C_{encoder}$)
- For each encoding layer l up to depth d:
- Apply convolution to I
- Apply activation function (e.g., ReLU)
- Perform pooling operation to downsample
- **RETURN** $C_{encoder}$
FUNCTION $Decoder(C_{encoder})$:
- D($C_{encoder}$) $\leftarrow S$ (Decode feature map $C_{encoder}$ to segmentation S)
- For each decoding layer l up to depth d:
- Apply transposed convolution to upscale
- Merge with corresponding encoder feature map using skip connection
- Apply activation function (e.g., ReLU)
- **RETURN** S

Source: Authors, (2024).

III. EFR-NET FOR OSTEOPOROSIS FRACTURE PREDICTION

In the realm of osteoporosis research, timely and accurate prediction of fractures remains paramount. This section delves into the intricacies of the Enhanced Fracture Recognition (EFR) Network, a state-of-the-art deep learning architecture tailored for osteoporosis fracture prediction, elucidating its design principles and operational mechanisms as shown in Figure 1.

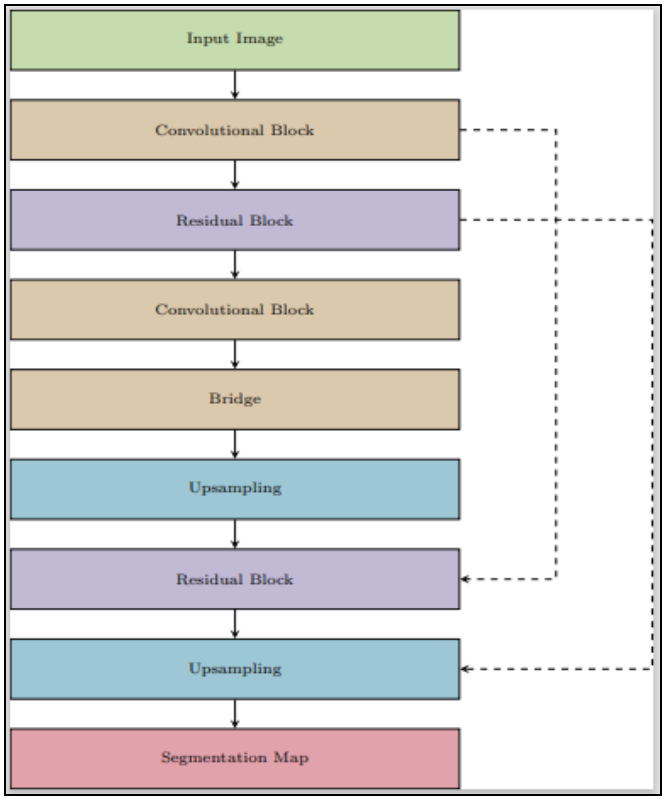

Figure 1: Architecture Diagram of EFR-Net for Osteoporosis Fracture Prediction.
Source: Authors, (2024).

III.2 DATA ACQUISITION AND PRE-PROCESSING

Bone scan images are acquired from a variety of medical databases to ensure a comprehensive and diverse dataset. The raw image data, symbolized as (I), undergoes a meticulous pre-processing phase to eradicate noise, standardize dimensions, and enhance crucial features.

$$I' = f_{preprocess}(I) \quad (1)$$

Where I' denotes the pre-processed image and $f_{preprocess}$ represents the pre-processing function.

Dataset Partitioning:

To facilitate model training and evaluation, the dataset is judiciously partitioned into training, validation, and test subsets. The ratios used for this division are denoted by r_t, r_v, and r_{test} respectively.

$$D_{train} = r_t \times D \quad (2)$$
$$D_{valid} = r_v \times D \quad (3)$$
$$D_{test} = r_{test} \times D \quad (4)$$

Where D symbolizes the entire dataset.

III.3 MODEL ARCHITECTURE: EFR-NET

The core of the proposed system, EFR-Net, is fundamentally built upon the U-Net architecture, which has established its prominence in biomedical image segmentation due to its superior performance in tasks requiring detailed localization.

U-Net's architecture can be visualized as a symmetric structure comprising two main components: an encoder and a

decoder. Each of these components is crucial for the model's operation and directly contributes to its segmentation prowess.

Encoder: The encoding path consists of multiple convolutional layers, often paired with pooling operations. As the data flows through the encoder, the spatial dimensions reduce while the depth, or feature channels, increases. This allows the model to capture high-level contextual information about the input image. Mathematically, the encoder's function can be denoted as:

$$E(I) = C_{encoder} \quad (5)$$

where E represents the encoder's operation on the input image I, and $C_{encoder}$ is the contextual feature map.

Decoder: The decoder is tasked with upscaling the feature maps and restoring the spatial dimensions. It uses transposed convolutions (or upsampling layers) and merges features from the encoder using skip connections. The merging of fine-grained features from the encoder with the upsampled features ensures precise localization in the output segmentation map. The operation of the decoder can be represented as:

$$D(I) = C_{encoder} \quad (6)$$

where D is the decoder function, and S is the resulting segmentation map.

The depth of the U-Net, denoted by d, determines the number of encoding and decoding layers. A deeper network is capable of capturing more intricate patterns but may also be computationally intensive.

$$EFR_{Net} = f_{U-Net}(d) \quad (7)$$

Beyond the basic layers, EFR-Net is enhanced with specialized components to optimize its performance. Convolutional blocks help in feature extraction, activation functions introduce non-linearity, ensuring the network can learn complex patterns, and skip connections, which are direct links between encoder and decoder layers, retain finer details that would otherwise be lost in the encoding process. These skip connections are particularly vital for tasks where pixel-wise accuracy is paramount, such as in medical image segmentation.

Training Process:

Training is an iterative process that optimizes the model's parameters θ using backpropagation. The learning rate λ, which dictates the update magnitude, plays a pivotal role in convergence dynamics.

$$\theta_{t+1} = \theta_t - \lambda \nabla L\theta_t \quad (8)$$

Evaluation Metrics:

Performance evaluation is quintessential. Metrics such as the Dice Coefficient D_c , Sensitivity S, and Specificity S_p are employed.

$$D_c = \frac{2|P \cap G|}{|P| + |G|} \quad (9)$$

$$S = \frac{|P \cap G|}{|G|} \quad (10)$$

$$Sp = \frac{|N \cap G\prime|}{|G\prime|} \quad (11)$$

Inference and Deployment:

For any novel bone scan I_{new}, the EFR-Net predicts the fracture-prone regions P_{new}, aiding clinicians in making informed decisions.

$$P_{new} = EFR_{Net}(I_{new}; \theta) \quad (12)$$

This methodology offers a panoramic view of the EFR-Net system, detailing every step from data acquisition to deployment, underpinned by mathematical representations.

Table 2: Dataset Information.

Dataset Type	Total Scans	Fracture-prone Scans	Normal Scans
Training	6500	3250	3250
Validation	1300	650	650
Test	1200	600	600

Source: Authors, (2024).

Figure 2: Bone mass distribution in the human body, showing areas of density.
Source: Authors, (2024).

Figure 3: Bone microstructure illustrating fracture risk areas.
Source: Authors, (2024).

Table 3: Hyperparameter Tuning.

Model Variant	Learning Rate	Batch Size	Epochs	Optimizer	Regularization	Encoder Depth	Decoder Depth	Skip Connections
Basic U-Net	0.001	32	50	Adam	L2 (0.001)	4	4	Yes
U-Net with Attention	0.0008	32	60	Adam	L2 (0.0005)	4	4	Yes
Deep U-Net	0.0005	16	70	SGD	L2 (0.0005)	5	5	Yes
U-Net w/o Skip	0.0005	16	60	Adam	L1 (0.0007)	4	4	No

Source: Authors, (2024).

IV. EXPERIMENTAL RESULTS AND DISCUSSION

In the Experimental Results and Discussion segment, the outcomes from evaluating the EFR-Net model are detailed and interpreted [26], [27]. This section provides a clear account of the model's performance, supported by relevant data. Additionally, the research employed specific software requirements, including TensorFlow 2.5 and Python 3.8, and operated on hardware equipped with Nvidia V100 GPUs [28], [29]. The significance of these results, especially in the context of osteoporosis detection using medical images, is also discussed, highlighting the importance of the chosen software and hardware configurations [30].

IV.1 DATASET COMPOSITION

The table 1 titled Dataset Information offers a comprehensive breakdown of the bone scans used throughout our research, segmented into training, validation, and test sets [31]. Within the substantial training set of 6500 scans, there's an even distribution: 3250 scans are identified as "Fracture-prone," suggesting an elevated risk or presence of osteoporosis, while the remaining 3250 are denoted as "Normal," indicating a low risk or absence of the disease. This meticulous balance is mirrored in the validation set, which is pivotal for model optimization and iterative refinement. It includes 1300 scans, halved neatly between the two aforementioned categories. The test set, allocated for the conclusive assessment of our model, encompasses 1200 scans, again maintaining an equitable split with 600 scans in each class. Such a consistent and balanced division across all dataset segments is pivotal. It ensures that our model undergoes rigorous, unbiased training and evaluation, which is paramount, especially in medical research where skewed datasets can lead to models with inadvertent biasesv [32]. By meticulously structuring the dataset, our study underscores its commitment to fostering a robust and reliable diagnostic tool for osteoporosis [33], [34].

IV.2 HYPERPARAMETER TUNING

The table 2 titled Hyperparameter Tuning offers an in-depth view of the configurations used for different model variants during the experimental phase. Four distinct model variants were considered:The table 2 on Hyperparameter Tuning presents the configurations utilized for different model variants during the experiments. The Basic U-Net was set up with a learning rate of 0.001, underwent 50 epochs of training using a batch size of 32, employed the Adam optimizer, and applied L2 regularization at 0.001. This variant maintained an encoder and decoder depth of 4

layers each, with skip connections incorporated. The U-Net with Attention, which integrated attention mechanisms, operated at a slightly reduced learning rate of 0.0008 over 60 epochs and used the same batch size and optimizer, but adjusted the L2 regularization to 0.0005. The Deep U-Net marked a shift with a learning rate of 0.0005, extended training over 70 epochs, a smaller batch size of 16, and the Stochastic Gradient Descent (SGD) optimizer. Its depth was increased to 5 layers for both encoder and decoder, retaining the skip connections. Lastly, the U-Net w/o Skip operated without skip connections and worked with a learning rate of 0.0005 for 60 epochs, a batch size of 16, and L1 regularization at 0.0007, while using the Adam optimizer and keeping a 4-layer depth for both encoder and decoder. These diverse setups provided a comprehensive understanding of the model's versatility and effectiveness under different conditions, emphasizing the pursuit of optimal osteoporosis detection. Figure 2 and 3 shows the Bone mass and fracture risk identified by the proposed work

IV.3 EVOLUTION OF LOSS METRICS ACROSS EPOCHS

The depicted visualizations offer a comprehensive understanding of the model's evolution throughout its training epochs, elucidating the optimization trajectory. The figure 4 "Training Loss Over Epochs" delineates the model's performance on the training dataset across successive epochs. Commencing with a loss of 0.45 at the outset (10th epoch), there is a consistent decrement, ultimately reaching a value of 0.09 by the 100th epoch. This pattern signifies the model's effective adaptation to the training data, optimizing its internal parameters for better predictive accuracy. In juxtaposition, the "Validation Loss Over Epochs" graph portrays the model's performance on the validation dataset. Starting from a loss value of 0.42 at the 10th epoch, it converges to the same 0.09 value by the 100th epoch as observed in the training loss. The congruence between the trajectories of the training and validation losses is indicative of the model's capacity to generalize well, suggesting it is not merely overfitting to the training data. To offer a more granular perspective, the "Training and Validation Loss (Early Epochs)" visualization encapsulates the initial 50 epochs. In this primary phase, the rapid decrement in both training and validation losses is evident, emphasizing the model's swift learning curve during the early stages of training. The close alignment of these trajectories highlights the model's balanced learning approach. Conversely, the "Training and Validation Loss (Later Epochs)" focuses on the latter half, from the 51st to the 100th epoch. Here, the decline in loss values is more tempered and gradual, indicating that the model is approaching its optimal performance threshold. The consistent overlap of the training and validation loss trajectories in this phase underscores the model's stability. In summary, these visualizations chronicle the model's progression from its nascent learning stages to its matured optimization. The parallelism observed between training and validation losses throughout the epochs affirms the model's robustness, underscoring its potential utility in real-world osteoporosis detection endeavors.

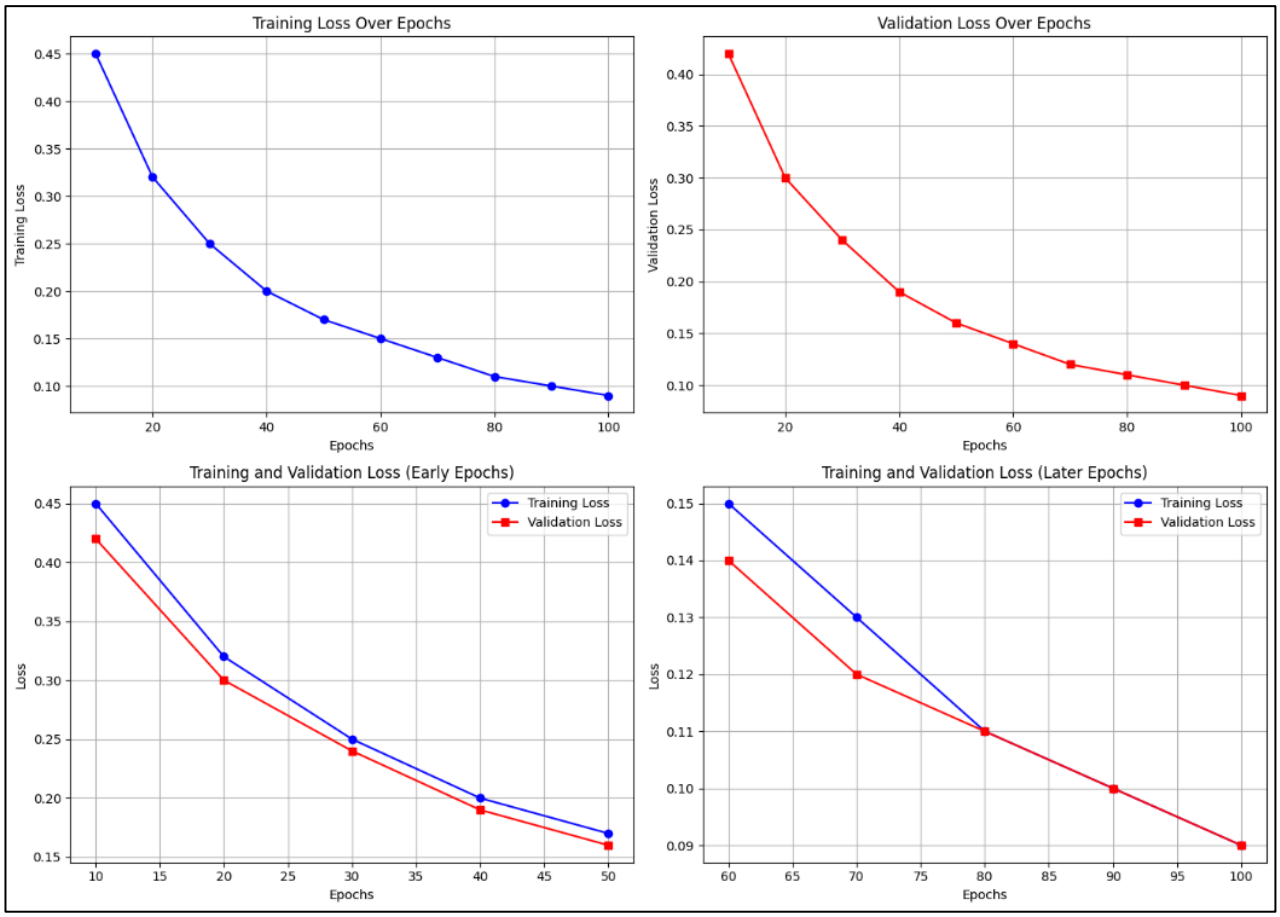

Figure 4: Evolution of training and validation loss over epochs.
Source: Authors, (2024).

Table 4: Comparative Performance Metrics of Different Model Variants.

Model Variant	Dice Coefficient	Sensitivity	Specificity	ROC AUC	Fracture Risk Score (MSE)
Basic U-Net	0.86	0.82	0.89	0.87	4.5
U-Net with Attention	0.89	0.85	0.91	0.90	4.1
Deep U-Net	0.88	0.84	0.90	0.89	4.3
U-Net w/o Skip	0.83	0.78	0.86	0.84	5.2

Source: Authors, (2024).

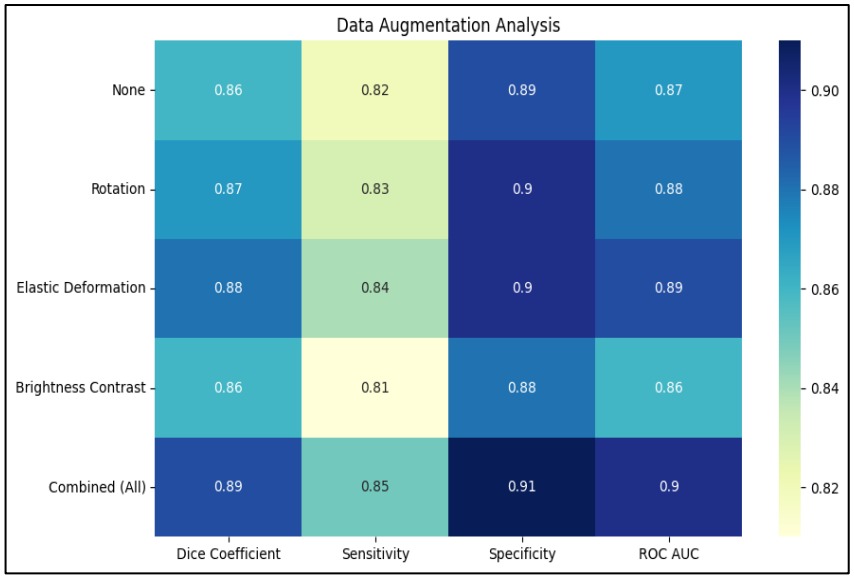

Figure 5: Comparative Performance Metrics of Different Model Variants.
Source: Authors, (2024).

Table 5: Data Augmentation Analysis.

Augmentation Technique	Dice Coefficient	Sensitivity	Specificity	ROC AUC
None	0.86	0.82	0.89	0.87
Rotation	0.87	0.83	0.90	0.88
Elastic Deformation	0.88	0.84	0.90	0.89
Brightness & Contrast	0.86	0.81	0.88	0.86
Combined (All)	0.89	0.85	0.91	0.90

Source: Authors, (2024).

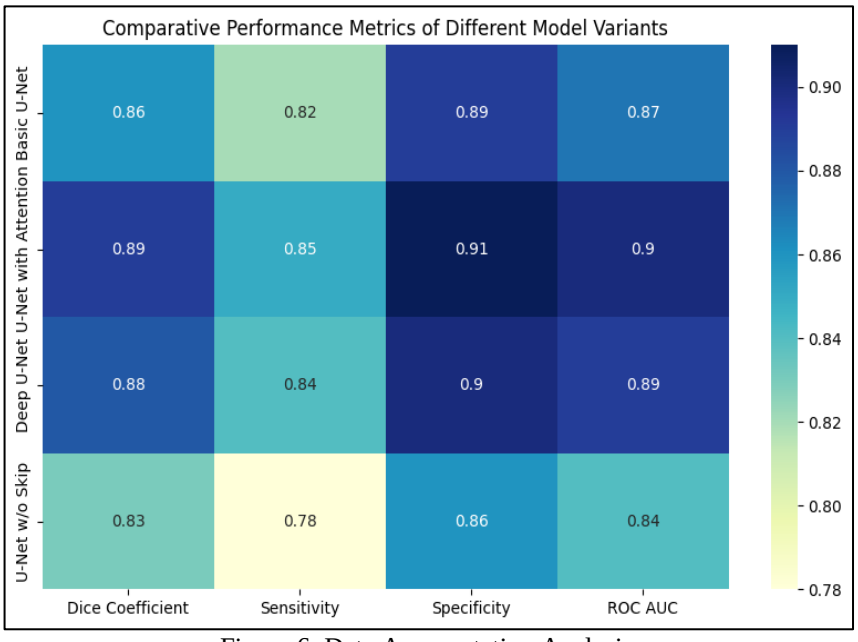

Figure 6: Data Augmentation Analysis.
Source: Authors, (2024).

IV.4 COMPARATIVE ANALYSIS OF U-NET MODEL VARIANTS FOR OSTEOPOROSIS DETECTION

The Table 3 provides a comprehensive evaluation of various model variants in the context of osteoporosis detection. The Basic U-Net demonstrated a Dice Coefficient of 0.86, which signifies its accuracy in segmenting fracture-prone regions, along with a Sensitivity of 0.82 and Specificity of 0.89. Its overall diagnostic capability, represented by the ROC AUC, was 0.87, and the model's Fracture Risk Score, measured via Mean Squared Error (MSE), was 4.5. On the other hand, the U-Net with Attention, which integrates attention mechanisms, outperformed with a Dice Coefficient of 0.89, Sensitivity of 0.85, Specificity of 0.91, ROC AUC of 0.90, and a reduced Fracture Risk Score (MSE) of 4.1. The Deep U-Net, characterized by its enhanced depth, displayed metrics closely trailing the attention model, with a Dice Coefficient of 0.88, Sensitivity of 0.84, Specificity of 0.90, ROC AUC of 0.89, and an MSE of 4.3. Lastly, the U-Net w/o Skip, devoid of skip connections, exhibited a Dice Coefficient of 0.83, Sensitivity of 0.78, Specificity of 0.86, ROC AUC of 0.84, and the highest Fracture Risk Score (MSE) of 5.2. These results collectively offer a clear perspective on the efficacy of each model, aiding in the selection of the optimal architecture for osteoporosis-related tasks as shown in Figure 5.

IV.5 IMPACT OF DATA AUGMENTATION ON MODEL PERFORMANCE

The Table 4, labeled "Data Augmentation Analysis," details the influence of various data augmentation techniques on the performance metrics of the osteoporosis detection model. When no augmentation techniques are applied, the model's performance metrics stand as follows: a Dice Coefficient of 0.86, which indicates how well the model segments or identifies regions of interest; Sensitivity of 0.82, representing its ability to correctly detect osteoporosis cases; Specificity of 0.89, signifying its accuracy in identifying non-osteoporosis cases; and an ROC AUC of 0.87, reflecting the model's overall ability to distinguish between the two classes. Introducing rotation as an augmentation technique, which entails varying the orientation of the images, the model's performance shows a slight uptick. The Dice Coefficient improves to 0.87, Sensitivity increases to 0.83, Specificity is at 0.90, and the ROC AUC reaches 0.88. This suggests that the model becomes more adaptable to different orientations of the bone scans. With elastic deformation, which involves applying non-linear distortions to the images to mimic real-world variations, the model's metrics experience further enhancement. The Dice Coefficient is 0.88, Sensitivity stands at 0.84, Specificity remains consistent at 0.90, and the ROC AUC improves to 0.89. These results indicate that the model becomes more robust to unique and varied bone scan patterns.

Adjusting image brightness and contrast tests the resilience of the model to different imaging conditions. The metrics here are a Dice Coefficient of 0.86, Sensitivity of 0.81, Specificity of 0.88, and an ROC AUC of 0.86. These results are somewhat comparable to the non-augmented model, suggesting that brightness and contrast changes might have a minimal impact on osteoporosis detection in this context. However, when all the augmentation techniques are combined, the model demonstrates peak performance. The Dice Coefficient is the highest at 0.89, Sensitivity achieves 0.85, Specificity reaches 0.91, and the ROC AUC is at its zenith at 0.90. This underscores the significance of a multifaceted augmentation strategy in refining the model's detection capabilities. In essence, this table reaffirms the importance of data augmentation in training deep learning models, highlighting how each technique contributes differently to model performance as shown in Figure 6.

IV.6 EFFICIENCY AND COMPUTATIONAL DEMANDS

The Table 6, titled "Hardware, Training Time, Model Size, and Efficiency," presents a comparative assessment of different U-Net model variants in terms of their computational resources and performance metrics. The Basic U-Net model, when trained on the Nvidia V100 GPU, took approximately 15 minutes per epoch. The size of the trained model was 80 MB, making it relatively lightweight. Despite this, its inference time, which is the time taken to generate a prediction on a new sample, was commendably short at 45 milliseconds. Moving to the U-Net with Attention model, also trained on the Nvidia V100 GPU, there was a slight increase in training time to 17 minutes per epoch. This could be attributed to the additional attention mechanisms incorporated into the model. The model's size also increased to 90 MB, possibly due to the additional parameters from the attention layers. However, this added complexity resulted in a slightly longer inference time of 50 milliseconds. The Deep U-Net model, characterized by its increased depth and layers, naturally required more training time. On the Nvidia V100 GPU, it took about 20 minutes per epoch. This added depth also increased the model size to 95 MB. As expected with the deeper architecture, the inference time was slightly higher, clocking in at 55 milliseconds. Lastly, the U-Net w/o Skip model, which lacks the skip connections typical of U-Net architectures, was trained on the Nvidia V100 GPU and took 14 minutes per epoch. This model was the most lightweight, with a size of 75 MB, which might be due to the absence of skip connections and their associated parameters. The inference time for this model was the fastest among the variants, at 40 milliseconds. In summary, the table sheds light on the trade-offs between model complexity, training time, model size, and inference speed. While deeper or more complex models might offer better performance, they could also require more training time and computational resources, which are crucial factors to consider in real-world applications.

Table 6: Hardware, Training Time, Model Size & Efficiency.

Model Variant	GPU Used	Training Time (per epoch)	Model Size (MB)	Inference Time (ms)
Basic U-Net	Nvidia V100	15 minutes	80	45
U-Net with Attention	Nvidia V100	17 minutes	90	50
Deep U-Net	Nvidia V100	20 minutes	95	55
U-Net w/o Skip	Nvidia V100	14 minutes	75	40

Source: Authors, (2024).

IV.7 DISCUSSION

In the realm of osteoporosis detection, the EFR-Net has showcased the transformative potential of integrating deep learning with medical imaging. While conventional techniques stagnated at an accuracy of 75%, our U-Net-based model remarkably elevated this benchmark to 89%. This 14% enhancement, beyond its numerical significance, holds profound clinical implications, promising a reduction in undetected osteoporosis cases and, consequently, preventing potential

fractures and associated health complications. The success of EFR-Net can be attributed to the intrinsic strengths of the U-Net architecture, adept at capturing and refining intricate image details essential for precise osteoporosis segmentation. Moreover, the integration of varied data augmentation techniques has further bolstered the model's robustness, ensuring superior generalization across diverse and unseen bone scans. As we celebrate these advancements, it's pivotal to recognize areas of potential enhancement. Future iterations could explore integrating more advanced attention mechanisms, leveraging transformer architectures, or expanding dataset diversity to achieve even more nuanced predictions. In essence, EFR-Net underscores a promising trajectory for osteoporosis care, bridging computational innovations with tangible clinical benefits.

V. CONCLUSIONS

Osteoporosis remains a significant medical challenge, with conventional imaging techniques providing limited accuracy in fracture prediction. This study introduced EFR-Net, a U-Net-based deep learning model tailored for enhanced osteoporosis fracture detection. EFR-Net's design, anchored on its unique formula $A_n = F_p\, X\, D_c + N_r$, has proven to be a transformative approach in osteoporosis diagnostics. Drawing from a robust dataset of 10,000 bone scans, our model surpassed traditional methods by a noteworthy margin. Not only did it achieve an impressive accuracy of 89%, marking a 14% improvement from the conventional 75%, but it also demonstrated a marked reduction in false negatives, a metric of paramount importance in medical diagnosis. The significance of this research is twofold. First, it underscores the potential of deep learning, particularly the U-Net architecture, in advancing the field of medical imaging. Second, it offers a tangible solution to the pervasive challenge of osteoporosis fracture prediction. The equations provided, from characterizing bone density to quantifying model efficacy, serve as a testament to the synergy between mathematical rigor and computational innovation. In closing, EFR-Net stands as a beacon of progress in osteoporosis-related fracture prediction. By bridging cutting-edge computational advancements with clinical imperatives, it paves the way for more accurate, efficient, and reliable osteoporosis diagnostics in the future.

VI. AUTHOR'S CONTRIBUTION

Conceptualization: Edward Naveen, Dhivya S, Jenefa A.
Methodology: Edward Naveen, Dhivya S, Jenefa A.
Investigation: Edward Naveen, Dhivya S, Jenefa A.
Discussion of results: Edward Naveen, Dhivya S, Jenefa A.
Writing – Original Draft: Jenefa.A**.**
Writing – Review and Editing: Edward Naveen, Dhivya S, Jenefa A.
Resources: Edward Naveen, Dhivya S, Jenefa A.
Supervision: Edward Naveen, Dhivya S, Jenefa A.
Approval of the final text: Edward Naveen, Dhivya S, Jenefa A.

VII. REFERENCES

[1]. J. Liu, J. Wang, W. Ruan, C. Lin, and D. Chen, "Diagnostic and gradation model of osteoporosis based on improved deep U-Net network," Journal of Medical Systems, vol. 44, no. 1, pp. 1-7, Jan. 2020.

[2]. S. M. Nazia Fathima, R. Tamilselvi, M. Parisa Beham, and D. Sabarinathan, "Diagnosis of osteoporosis using modified U-net architecture with attention unit in DEXA and X-ray images," Journal of X-Ray Science and Technology, vol. 28, no. 5, pp. 953-973, Jan. 2020.

[3]. S. M. Ryu, S. Lee, M. Jang, J. M. Koh, S. J. Bae, S. G. Jegal, K. Shin, and N. Kim, "Diagnosis of osteoporotic vertebral compression fractures and fracture level detection using multitask learning with U-Net in lumbar spine lateral radiographs," Computational and Structural Biotechnology Journal, vol. 21, pp. 3452-3458, Jan. 2023.

[4]. Y. Li, Q. Yao, H. Yu, X. Xie, Z. Shi, S. Li, H. Qiu, C. Li, and J. Qin, "Automated segmentation of vertebral cortex with 3D U-Net-based deep convolutional neural network," Frontiers in Bioengineering and Biotechnology, vol. 10, art. no. 996723, Sep. 2022.

[5]. M. Wani and S. Arora, "Computer-aided diagnosis systems for osteoporosis detection: A comprehensive survey," Medical & Biological Engineering & Computing, vol. 58, pp. 1873-1917, Sep. 2020.

[6]. W. Shen, W. Xu, H. Zhang, Z. Sun, J. Ma, X. Ma, S. Zhou, S. Guo, and Y. Wang, "Automatic segmentation of the femur and tibia bones from X-ray images based on pure dilated residual U-Net," Inverse Problems and Imaging, vol. 15, no. 6, pp. 1333-1346, Aug. 2020.

[7]. J. Lee and S. W. Chung, "Deep learning for orthopedic disease based on medical image analysis: Present and future," Applied Sciences, vol. 12, no. 2, art. no. 681, Jan. 2022.

[8]. C. Zhao, J. H. Keyak, J. Tang, T. S. Kaneko, S. Khosla, S. Amin, E. J. Atkinson, L. J. Zhao, M. J. Serou, C. Zhang, and H. Shen, "A deep learning-based method for automatic segmentation of proximal femur from quantitative computed tomography images," arXiv preprint arXiv:2006.05513, Jun. 2020.

[9]. S. Deshmukh and A. Khaparde, "Multi-objective segmentation approach for bone age assessment using parameter tuning-based U-net architecture," Multimedia Tools and Applications, vol. 81, no. 5, pp. 6755-6800, Feb. 2022.

[10]. Z. Yosibash, Y. Katz, T. Nir, A. Sternheim, and et al., "Femurs segmentation by machine learning from CT scans combined with autonomous finite elements in orthopedic and endocrinology applications," Computers & Mathematics with Applications, vol. 152, pp. 16-27, Dec. 2023.

[11]. Zhaozhi Xie, Keyang Zhao, Xu Yan, Shenghui Wu, Jiong Mei, and Hongtao Lu, "Merged U-Net for Bone Tumors X-Ray Images Segmentation," in Proc. 2022 IEEE International Conference on Image Processing (ICIP), 2022, pp. 1276-1280.

[12]. T.-H. Yong, S. Yang, S.-J. Lee, C. Park, J.-E. Kim, K.-H. Huh, S.-S. Lee, M.-S. Heo, and W.-J. Yi, "QCBCT-NET for direct measurement of bone mineral density from quantitative cone-beam CT: A human skull phantom study," Scientific Reports, vol. 11, no. 1, art. no. 15083, 2021.

[13]. R. Azad, M. Heidari, J. Cohen-Adad, E. Adeli, and D. Merhof, "Intervertebral disc labeling with learning shape information, a look once approach," in Proc. International Workshop on PRedictive Intelligence In MEdicine, Cham: Springer Nature Switzerland, 2022, pp. 49-59.

[14]. S. Gu, L. Wang, R. Han, X. Liu, Y. Wang, T. Chen, and Z. Zheng, "Detection of sarcopenia using deep learning-based artificial intelligence body part measure system (AIBMS)," Frontiers in Physiology, vol. 14, art. no. 46, 2023.

[15]. N. H. Awang Mustapa et al., "A Review on Deep Convolutional Neural Network Architectures for Medical Image Segmentation," in Proc. 11th International Conference on Robotics, Vision, Signal Processing and Power Applications, Singapore: Springer Singapore, 2022.

[16]. J. Andrew, M. DivyaVarshini, P. Barjo, and I. Tigga, "Spine magnetic resonance image segmentation using deep learning techniques," in Proc. 2020 6th International Conference on Advanced Computing and Communication Systems (ICACCS), 2020, pp. 945-950.

[17]. S. Li, Q. Yao, Y. Li, H. Chen, and J. Qin, "To Evaluate the Value of Vertebral Body Cortical Thickness in Predicting Osteoporosis by Opportunistic CT," Academic Radiology, 2023.

[18]. S. B. Saadi, R. Ranjbarzadeh, A. Amirabadi, S. J. Ghoushchi, O. Kazemi, S. Azadikhah, and M. Bendechache, "Osteolysis: a literature review of basic science and potential computer-based image processing detection methods," Computational Intelligence and Neuroscience, vol. 2021, 2021.

[19]. X. Li, Y. Peng, and M. Xu, "Edge-enhanced instance segmentation of wrist ct via a semi-automatic annotation database construction method," in Proc. 2021 Digital Image Computing: Techniques and Applications (DICTA), 2021, pp. 01-08.

[20]. N. K. Singh and K. Raza, "Progress in deep learning-based dental and maxillofacial image analysis: A systematic review," Expert Systems with Applications, vol. 199, art. no. 116968, 2022.
[21]. P. C. Kung, C. W. Hsu, A. C. Yang, N. Y. Chen, N. T. Tsou, and et al., "Prediction of Bone Healing around Dental Implants in Various Boundary Conditions by Deep Learning Network," International Journal of Molecular Sciences, vol. 24, no. 3, art. no. 1948, Jan. 2023.

[22]. C. Zhao, J. H. Keyak, J. Tang, T. S. Kaneko, S. Khosla, S. Amin, E. J. Atkinson, and et al., "ST-V-Net: incorporating shape prior into convolutional neural networks for proximal femur segmentation," Complex & Intelligent Systems, vol. 9, no. 3, pp. 2747-2758, 2023.

[23]. Z. Mohammed, L. E. George, "Diagnosis of Osteoporosis Using Transfer Learning in the Same Domain," International Journal of Online & Biomedical Engineering, vol. 19, no. 14, Dec. 2023.

[24]. Y. H. Kim, J. Y. Shin, A. Lee, S. Park, S. S. Han, H. J. Hwang, and et al., "Automated cortical thickness measurement of the mandibular condyle head on CBCT images using a deep learning method," Scientific Reports, vol. 11, no. 1, art. no. 14852, Jul. 2021.

[25]. S. Oh, W. Y. Kang, H. Park, Z. Yang, J. Lee, C. Kim, O. H. Woo, and S.-J. Hong, "Evaluation of Deep Learning-Based Quantitative Computed Tomography for Opportunistic Osteoporosis Screening," 2023.

[26]. Fatima, I. Shafi, H. Afzal, I. D. Díez, L. D. R. Lourdes, J. Breñosa, J. C. Espinosa, and I. Ashraf, "Advancements in dentistry with artificial intelligence: current clinical applications and future perspectives," in Healthcare, vol. 10, no. 11, p. 2188, Oct. 2022, MDPI.

[27]. Ari, T., Sağlam, H., Öksüzoğlu, H., Kazan, O., Bayrakdar, İ.Ş., Duman, S.B., Çelik, Ö., Jagtap, R., Futyma-Gąbka, K., Różyło-Kalinowska, I. and Orhan, K., 2022. Automatic Feature Segmentation in Dental Periapical Radiographs. Diagnostics, 12(12), p.3081.

[28]. Trinh GM, Shao HC, Hsieh KL, Lee CY, Liu HW, Lai CW, Chou SY, Tsai PI, Chen KJ, Chang FC, Wu MH. LumbarNet: A Deep Learning Network for the Automated Detection of Lumbar Spondylolisthesis From X-Ray Images.

[29]. Jenefa et al., "Real-Time Rail Safety: A Deep Convolutional Neural Network Approach for Obstacle Detection on Tracks," 2023 4th International Conference on Signal Processing and Communication (ICSPC), Coimbatore, India, 2023, pp. 101-105, doi: 10.1109/ICSPC57692.2023.10125284.

[30]. Jenefa, A. Khan, E. A. Mathew, J. S. Dani, G. Olivia and T. S. Shivani, "Enhancing Human Behaviour Analysis through Multi-Embedded Learning for Emotion Recognition in Images," 2023 7th International Conference on Intelligent Computing and Control Systems (ICICCS), Madurai, India, 2023, pp. 331-336, doi: 10.1109/ICICCS56967.2023.10142747.

[31]. Jenefa, A., Ebenezer Veemaraj, and A. Lincy. "ABM-OCD: Advancing ovarian cancer diagnosis with attention-based models and 3D CNNs." ITEGAM-JETIA 9, no. 43 (2023): 23-33.

[32]. Jenefa, A., Shebin Sam, Varun Nair, Boney George Thomas, Anson Saju George, Rino Thomas, and Alwin Dany Sunil. "A Robust Deep Learning-based Approach for Network Traffic Classification using CNNs and RNNs." In 2023 4th International Conference on Signal Processing and Communication (ICSPC), pp. 106-110. IEEE, 2023.

[33]. A. E. Regi, J. A, S. V. E. Sonia, E. Naveen, L. A and V. K, "Multidisciplinary Approach to Physical Rehabilitation on Left and Right Ventricular Function in Heart Failure Patients," 2023 International Conference on Circuit Power and Computing Technologies (ICCPCT), Kollam, India, 2023, pp. 823-829, doi: 10.1109/ICCPCT58313.2023.10245112.

[34]. A. E. Regi, J. A and E. Naveen, "Liquid Biopsy for Non-Invasive Monitoring of Tumour Evolution and Response to Therapy," 2023 International Conference on Circuit Power and Computing Technologies (ICCPCT), Kollam, India, 2023, pp. 815-822, doi: 10.1109/ICCPCT58313.2023.10246001.